https://dx.doi.org/10.1016/j.jpowsour.2022.231108

Microscale-Decoupled Charge-Discharge Reaction Sites for An Air Electrode with Abundant Triple-Phase Boundary and Enhanced Cycle Stability of Zn-Air Batteries

Yawen Dai[1], Jie Yu[1], Peng Tan[2,*], Chun Cheng[1], Tong Liu[1], Siyuan Zhao[1], Zongping Shao[3], Tianshou Zhao[4,*], Meng Ni[1,*]

[1]Department of Building and Real Estate, Research Institute for Sustainable Urban Development (RISUD) and Research Institute for Smart Energy (RISE), The Hong Kong Polytechnic University, Hung Hom, Kowloon 999077, Hong Kong, P. R. China

[2] Department of Thermal Science and Energy Engineering, University of Science and Technology of China, Heifei 230026, Anhui, P. R. China

[3]State Key Laboratory of Materials-Oriented Chemical Engineering, College of Chemical Engineering, Nanjing Tech University, No. 5 Xin Mofan Road, Nanjing 210009, P. R. China

[4]Department of Aerospace and Mechanical Engineering, Hong Kong University of Science and Technology, Clear Water Bay, Kowloon 999077, Hong Kong, P. R. China

[*]Corresponding Author

E-mail:

meng.ni@polyu.edu.hk (Meng Ni)

pengtan@ustc.edu.cn (Peng Tan)

metzhao@ust.hk (Tianshou Zhao)

Abstract

Decreasing the charge-discharge voltage gap and increasing the cycling stability is pivotal but challenging for the practical application of rechargeable Zn-air battery (ZAB). Until now, many efforts have been paid in the electrocatalyst development for the air electrode, but few works have been done on the electrode structure design which is quite import for the battery performance. Herein, we design a decoupled air electrode by integrating a hydrophilic mesh active for oxygen evolution reaction (OER) with a hydrophobic layer active for oxygen reduction reaction (ORR). The decoupled air electrode could separate the OER and ORR sites at microscale, which could alleviate the oxidative corrosion of the ORR layer along cycling. Meanwhile, it also shows adjustable contact angle by fancily changing the texture of the mesh, which enables the optimal hydrophilicity towards abundant triple phase boundary for superior discharge performance. The ZAB based on the decoupled air electrode exhibits a small initial voltage gap of 0.75 V at 10 mA cm^{-2}, and it was stably cycled for 240 h. This work provides a feasible strategy to simultaneously accelerate the electrochemical reaction and improve the electrode stability, and it could be inspiring for other multiphase reaction involved devices.

Keywords: air electrode structure design, triple phase boundary, cycle stability, oxidative corrosion, Zn-air battery

1. Introduction

Rechargeable Zn-air battery attracts much research interests due to the high intrinsic safety, large theoretical energy density, and low cost. It is regarded as one of the most promising candidates for the next generation energy storage devices. However, the large potential gap between charge and discharge causes the low energy efficiency, which impedes the implementation of Zn-air batteries [1-3]. The dominant potential loss is from the air electrodes according to previous studies [4,5]. Although many efforts have been paid in the electrocatalyst development for the air electrode, few works have been done on the electrode structure design which is quite important for the battery performance [6-9]. The discharge reaction of air electrodes, oxygen reduction reaction (ORR), is a triple-phase-participated reaction which occurs at the phase boundary between the liquid electrolyte, the solid electrode, and the gas phase O_2 reactant [10-12]. On the contrary, the charge reaction, oxygen evolution reaction (OER) occurs at the dual-phase boundary which favors the maximum contact between liquid and solid and fast desorption of gas phase O_2 product [13,14]. Hence, it is difficult to balance the hydrophobicity and hydrophilicity of the air electrode to simultaneously satisfy ORR and OER reactions [7,15,16]. In the previous studies, the dominant method to control the hydrophobicity is to add the hydrophobic additives such as polytetrafluoroethylene (PTFE) [15,17]. However, the low conductivity of PTFE highly impedes the electron transport [18]. Besides, PTFE could also adhere to the catalytic materials and block the active sites [19]. The two disadvantages greatly limit the discharge performance of Zn-air batteries. Therefore, developing a new strategy to adjust the hydrophobicity of air electrodes is quite important. Zhang's group reported an asymmetric air electrode which has a hydrophilic side facing to the electrolyte and a hydrophobic side facing to the air [20]. This unique structure significantly enlarged the triple-phase boundary from a conventional two-dimensional configuration to a three-dimensional region, and thus promoted the discharge performance of the air electrode. Cui's group designed a breathing-mimicking electrocatalytic system to realize amplified triple-phase boundary lines and dual-direction gas pathways for the O_2 evolution and consumption [21]. Shao's group developed a dual-layer structure of the air electrode which composed of a hydrophobic MnS layer and a hydrophilic Ni-Co-S layer, and it showed decreased charge voltage and increased discharge voltage in Zn-air batteries as compared to the single-layer structure [22].

In addition to the large charge-discharge voltage gap, the short cycle life is another critical obstacle that hinders the practical use of rechargeable Zn-air batteries [23-25]. The main reason of the degradation of the battery performance along cycling operation is the oxidative corrosion of the air electrode during the charging process [26,27]. The high OER potential could gradually oxidize the electrocatalysts, porous conductive carbon, and the gas diffusion layer, leading to the flooding of air electrode and the loss of triple phase boundary [2,28,29]. Regarding this problem, the three-electrode system was suggested to separate the charge and discharge reactions on two distinct electrodes, and thus the air electrode could be protected from the high OER potential [30-32]. However, the three-electrode system adds to the complexity of the device configuration and increases the weight and volume of the battery which reduces the real energy density. Wang et al. designed a Janus structure of the air electrode with separate distribution of OER and ORR electrocatalysts on two faces of the substrate, which realized the separation of charge and discharge reactions on one electrode, and thus improved the cycle stability [33]. However, the fabrication process of the Janus electrode required repeated coating and removing of polymers on the electrode, which is time consuming and may cause peeling of the active materials. Therefore, a facile method to fabricate an electrode with separate OER and ORR sites is still highly demanded.

The above analysis indicates that proper hydrophilicity and separate OER-ORR sites are two pivotal characteristics for a high performance and stable air electrode, but it is challenging to simultaneously regulate the two features. Herein, we designed a unique air electrode structure with adjustable hydrophilicity and microscale decoupled OER and ORR sites. We choose the conventional cheap materials of Mn_2O_3/C for ORR and $FeOOH/Ni(OH)_2$ for OER as the platform to demonstrate the concept of novel air electrode structure. The decoupled air electrode was produced by pressing a sprayed

Mn_2O_3/C layer with a FeOOH/$Ni(OH)_2$ coated steel mesh, and thus the ORR and OER active materials could be alternatively arranged on the air electrode surface with a meshed structure. Additionally, the texture of the catalytic surface could be tuned by changing the mesh density, realizing a free control of the contact angle within a large range from 63 º to 133 º, enabling the optimization of hydrophobicity towards the maximum triple phase boundary. This work reports a facile method to simultaneously achieve decoupled OER and ORR sites and optimal hydrophobicity of the air electrode, which is promising for further development of high-performance and long-stable rechargeable Zn-air batteries.

2. Experimental

2.1 Material synthesis and electrode fabrication

2.1.1 Coating $Ni(OH)_2$/FeOOH on stainless steel

The fabrication process of the decoupled air electrode is illustrated in Scheme 1. A stainless-steel mesh (type 304) was immersed in a 0.1 g mL^{-1} $FeCl_3$ solution and stirred in room temperature for 5 h. The acidic solution environment could assist partial surface oxidation of iron and nickel of the steel, leading to the formation of corresponding hydroxide [34,35]. After rinsing and natural drying, the activated steel mesh (named as a-Steel) was obtained.

2.1.2 Synthesis of Mn_2O_3 powder

The Mn_2O_3 powder was synthesized by a facile sol-gel method. Typically, 0.01 mol $Mn(CH_3COOH)_2$ was dissolved in 20 mL H_2O. 2.92 g ethylenediaminetetraacetic acid and 4.2 g citric acid were dissolved in 8 mL aqueous ammonia (25 wt%) and in 5 mL H_2O, and then the solution was dropwise added into the $Mn(CH_3COOH)_2$ solution to get a transparent mixture. The above mixture was heated on a hot plate until a white gel was obtained. The gel was carbonized under 180 □ for 12 h in oven in air, and then annealed at 600 □ for 5 h in air. The annealed powder was treated by 0.5 M HNO_3 for 4 h to partially etch the Mn-O motifs [36], and thus to decrease the particle size and to increase the surface area to get the final product of Mn_2O_3.

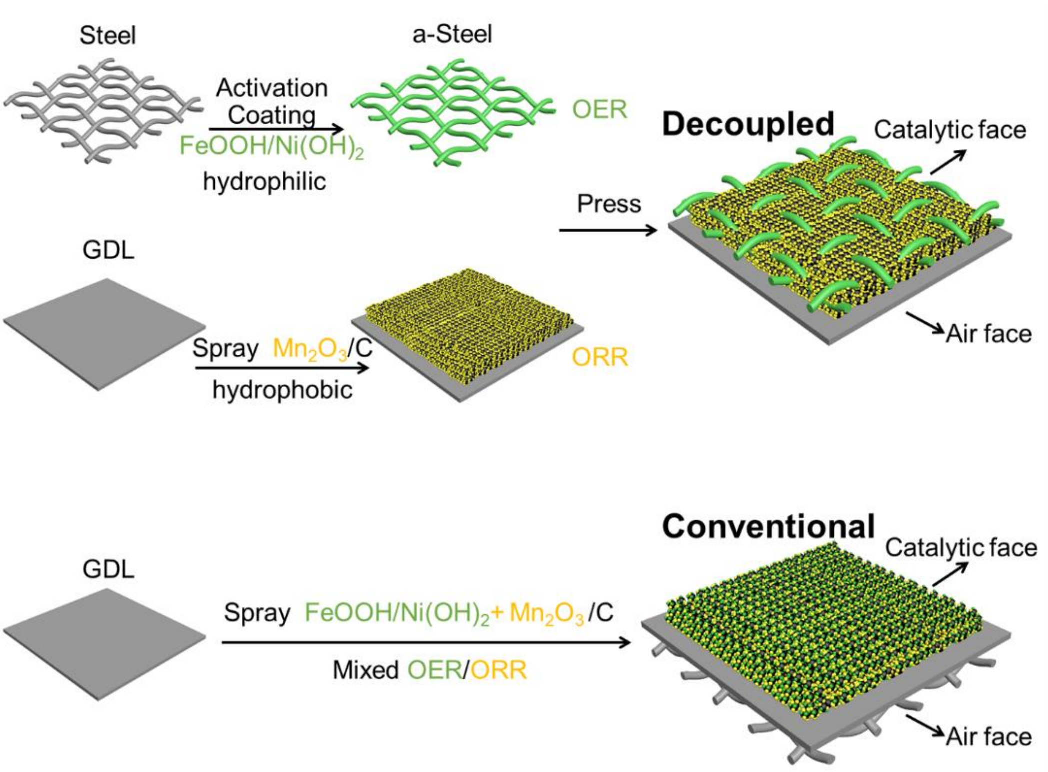

Scheme 1. Fabrication procedure of the decoupled air electrode and conventional air electrode.

2.1.3 Fabrication of the decoupled air electrode

The Mn_2O_3 powder was mixed with carbon support (XC 72) with a mass ratio of 2:1, then 5 wt% Nafion and absolute ethanol were added into the above mixed powder with a ratio of 60 μL : 1 mL : 15 mg. Ball-milling was then conducted at 400 rpm for 30 min for the mixture to get a homogenous ink. The ink was sprayed on a carbon paper (SGL-36BB) with a Mn_2O_3 mass loading of 2 mg cm^{-2}, after which the a-Steel was integrated onto the sprayed side by cold-press with 10 MPa pressure persisting for 30 s. Afterwards, another carbon paper (HCP020P) was packed on the backside of the above a-Steel/Mn_2O_3-C sprayed SGL-36BB during battery assembling to form the final decoupled air electrode with the configuration of a-Steel/Mn_2O_3-C/SGL-

36BB/HCP020P. The two layers of carbon papers (SGL 36BB for the catalytic face and HCP020P for the air face) function as the gas diffusion layer (GDL). The a-Steel could simultaneously act as the current collector linking to the external circuit.

2.1.4 Fabrication of the conventional air electrode

As a control, the conventional air electrode was fabricated. The powder $FeOOH/Ni(OH)_2$ was prepared by immersing nickel/iron powder in in a 0.1 g mL^{-1} $FeCl_3$ solution and stirred in room temperature for 5 h. The powder was then vacuum filtered and dried in oven. The unreacted metallic powder was separated from the hydroxide product by a magnet. $FeOOH/Ni(OH)_2$, Mn_2O_3, and XC-72 powders were mixed with a mass ratio of 1 : 1: 1, after which Nafion and ethanol were added, and balling milling were conducted to form a homogenous ink using the same condition as the decoupled air electrode preparation. The ink was then sprayed onto a carbon paper (SGL-36BB) with a mass loading of 2 mg cm^{-2} $FeOOH/Ni(OH)_2$ + 2 mg cm^{-2} Mn_2O_3. Afterwards, another carbon paper (HCP020P) was packed on the backside of the above $FeOOH/Ni(OH)_2$+Mn_2O_3-C sprayed SGL-36BB, and the two layers of carbon papers function as the GDL. An additional 400-mesh original type 304 stainless steel acting as the current collector was packed onto the HCP020P side. Furthermore, the noble metal benchmark catalysts were also used to fabricate the conventional air electrode as a control sample using the same procedure, and the mass loading was kept the same as 2 mg cm^{-2} RuO_2 + 2 mg cm^{-2} Pt/C (20 wt% Pt).

2.2 Characterization

The chemical identity of the materials was confirmed through Raman spectra recorded by a Renishaw micro-Raman spectroscopy system using the excitation wavelength of 532 nm and the laser intensity of 0.5 mW. The X-ray diffraction (XRD) patterns were acquired by an X-ray Diffractometer (Rigaku SmartLab 9kW - Advance).

The morphology of the air electrodes was observed by a TESCAN VEGA3 field scanning electron microscope (SEM) at the accelerating voltage of 20 kV. The elemental composition was investigated by the energy dispersive X-ray spectroscopy (EDX). The spatial distribution of materials on the electrode was studied by EDX-mapping and EDX-linear scan. The composition and chemical environment of the surface elements were detected by X-ray photoelectron spectroscopy (XPS) through a Nexsa XPS system. The contact angles were measured by capturing the static morphology of 1 μL H_2O on the surface of the horizontally placed samples.

2.3 Electrochemical activity and battery performance test

The electrochemical activity and stability of the material for ORR and OER half reactions were evaluated by a three-electrode system on a Solartron potentiostat. A rotating disk electrode (RDE), a graphite rod, and a Hg/HgO electrode were used as the working electrode, counter electrode, and reference electrode, respectively. O_2 saturated 0.1 M KOH was used as the electrolyte. The powder electrocatalysts was mixed with the conductive carbon (Super P Li) with a mass ratio of 2:1, and they are dispersed in the mixed ethanol/5 wt% Nafion with a volume ratio of 47:3 to get a suspension with a concentration of 10 mg_{cat} mL^{-1}. The suspension was ultrasonicated towards a homogenous ink and then dropped on the RDE to realize a catalyst loading of 0.5 mg_{cat} cm^{-2}. The linear scan voltammetry curves were recorded at a scan rate of 5 mV s^{-1}. The ORR and OER stability were assessed by chronoamperometric response at 0.3 V vs. RHE and chronopotentiometric response at 10 mA cm^{-2}, respectively.

For battery assembling, the as-prepared electrodes described in section 2.1 were used as the air electrode and the exposed areas towards the electrolyte side and air side were 0.785 cm^2. A zinc foil with exposed area of 7.065 cm^2 was used as the Zn electrode. The large Zn area aims at minimizing the polarization of Zn electrode, and thus to guarantee that the battery performance is dominated by the air electrode. The 6 M KOH+0.2 M $Zn(CH_3COO)_2$ solution was used as the electrolyte. The cell has a chamber volume of 7.065 ml to hold the electrolyte. The cell diagram is presented in **Fig. S1**. All the battery performance tests were carried out under ambient air. The electrochemical active surface areas (ECSA) of the air electrodes were evaluated by measuring the double layer capacitance (C_{dl}) through cyclovoltammetry within non-Faradic region (1.45 V to 1.60 V vs. Zn) at varied scan rate. The electrochemical impedance spectra (EIS) were collected under open circuit condition with the frequency range of 10^5 to 1 Hz. The rate performance and cycle stability were evaluated by recording the galvanostatic discharge and charge curves on a NEWARE testing system.

3. Result and Discussion

3.1 Chemical identity and electrochemical activity of the material

Fig. 1a shows the SEM image of the steel mesh, and the magnified SEM image (**Fig. 1b**) shows the smooth surface of the steel wire. After the activation treatment, the a-Steel sample with the preserved mesh structure and the rougher wire surface (**Fig. 1c**) is obtained. The phase identity of the materials is analyzed by the XRD patterns (**Fig. S2**). a-Steel shows the same XRD pattern with the original Steel, which is because of the small mass ratio of the surface species formed during the activation treatment. For the powder sample of $FeOOH/Ni(OH)_2$, the $Ni(OH)_2$ phase can be clearly recognized by the PDF card $Ni(OH)_2$#14-0117. No XRD peaks can be assigned to FeOOH, which might be due to the low crystallinity. The XRD pattern of Mn_2O_3 powder matches well with the PDF card of Mn_2O_3#41-1442. Raman spectra is further acquired to supplement the chemical nature identification. The Raman spectra (**Fig. 1d**) verify the mixed component of FeOOH (identified by the peak group at 219, 283, 397, 484, and 594 cm^{-1}) and $Ni(OH)_2$ (identified by the featured broad peak at 680 cm^{-1}), both of which are typical OER-active electrocatalysts [37]. The powder sample of FeOOH/Ni(OH)$_2$ shows identical Raman signals as the a-Steel, which ensures the reasonable comparison between the conventional air electrode and decoupled air electrode. The ORR-active Mn_2O_3 powder shows the characteristic Raman shift at 636 cm^{-1} [38].

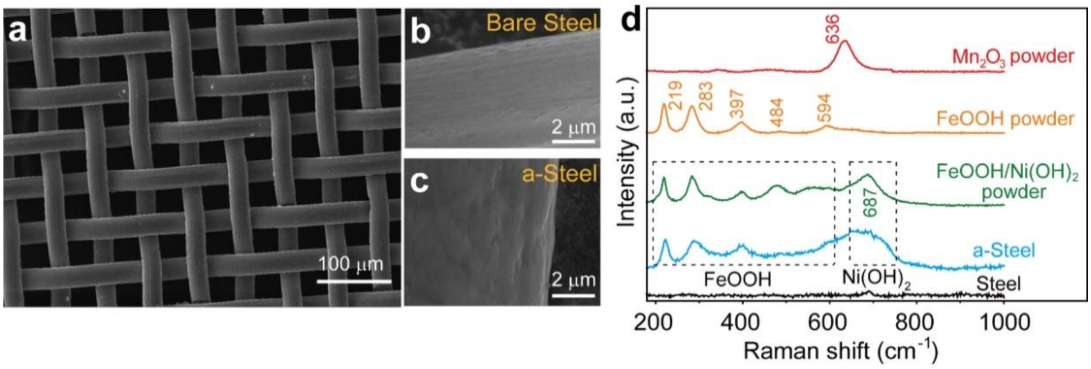

Fig. 1. (a) SEM images of the steel mesh, and the magnified SEM images of (b) the bare steel and (c) a-Steel. The scale bars in a, b, and c are 100 µm, 2 µm, and 2 µm, respectively. (d) Raman spectra of Mn_2O_3, FeOOH, FeOOH/Ni(OH)$_2$ powders, Steel, and a-Steel.

The electrocatalytic activity and stability of the as-synthesized materials and the noble metal benchmarks are shown in **Fig. 2**. In the ORR-LSV curves (**Fig. 2a**), Mn_2O_3 shows the limiting current density of 5.2 mA cm^{-2}, which is lower than the Pt/C with the same mass loading (5.8 mA cm^{-2}), but comparable to the Pt/C with half mass loading (**Fig. S3a**). Mn_2O_3 shows good ORR stability with a current retention of 84 % after 50 h in the chronoamperometry test at 0.3 V vs. RHE (**Fig. 2b**). Although it is not as good as Pt/C with the same mass loading (94%, 50h), it outperforms the Pt/C with half mass loading (75%, 20 h, **Fig. S3b**). Hence, Mn_2O_3 is more promising for large scale practical utilization than Pt/C. The OER-LSV curve (**Fig. 2c**) of the powder FeOOH/Ni(OH)$_2$ shows a potential of 1.58 V vs. RHE at 10 mA cm^{-2}, which is close to that of the benchmark RuO_2 (1.55 V vs. RHE). Moreover, the powder FeOOH/Ni(OH)$_2$ shows a stable chronopotentiometry profile at 10 mA cm^{-2} for 30 h with only a small potential increase of 0.04 V (**Fig. 2d**), whereas RuO_2 shows poor stability with large potential increase of 0.25 V in 10 h. The a-Steel shows consistently good OER activity with the powder $FeOOH/Ni(OH)_2$ (**Fig. 2e**), and it could be stably operated at 10 mA cm^{-2} for 200 h with a small potential increase of 0.04 V (**Fig. 2f**). The above test implies that the platform materials of Mn_2O_3 for ORR and $FeOOH/Ni(OH)_2$ for OER have qualified activity and stability for the concept demonstration of our decoupled air electrode structure.

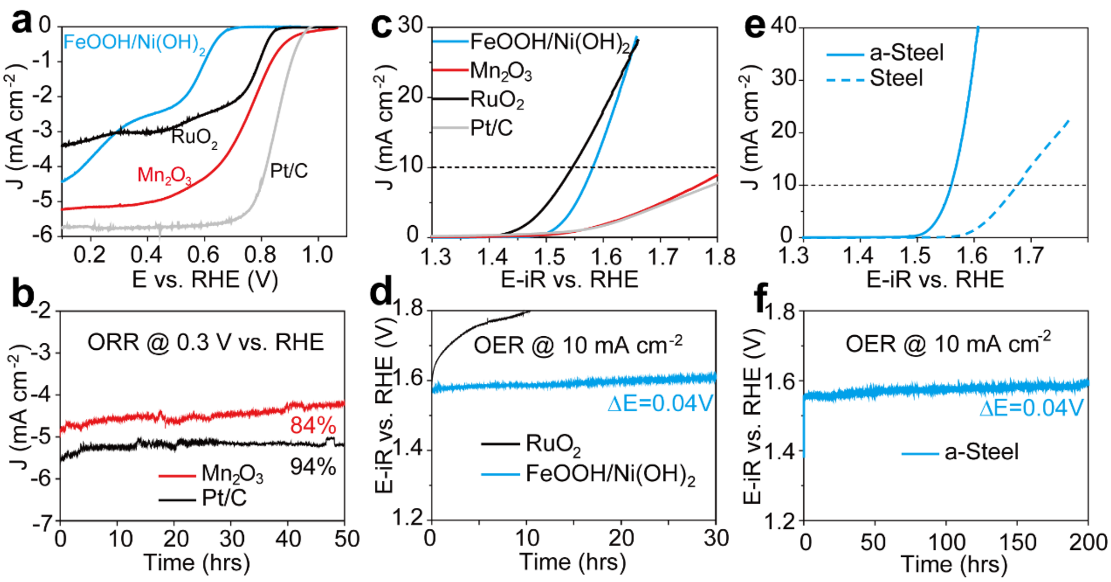

Fig. 2. (a) ORR-LSV curves of powder samples tested on RDE and (b) ORR current densities recorded at 0.3 V vs. RHE under chronoamperometry mode. (c) OER-LSV curves of the powder samples tested on RDE and (d) corresponding long-term stability test of OER potentials at 10 mA cm^{-2} under chronopotentiometry mode. The loading mass of powder catalysts on RDE is fixed at 0.5 mg cm^{-2}. (e) OER-LSV curves of Steel and a-Steel. (f) Chronopotentiometry OER potential response of a-Steel recorded at 10 mA cm^{-2}.

3.2 Morphology and spatial composition of the decoupled air electrode

The top-view SEM image of the decoupled air electrode (**Fig. 3a**) shows the mesh morphology of a-Steel packed with the underlying spayed layer. The cross-sectional SEM image (**Fig. 3b**) shows the electrode thickness of about 200 μm. The EDX spectrum (**Fig. 3c**) is extracted to study the elemental composition, which shows obvious signals of Mn and C from the sprayed layer, as well as Fe, Ni, Cr from the a-

Steel. The elemental mapping in **Fig. 3d** clearly presents the spatially separated distribution of Ni/Fe (active for OER) and Mn/C (active for ORR), suggesting the successful design of the microscale decoupled OER and ORR sites at the air electrode. The cross-sectional SEM image was magnified in **Fig. 3e and 3f**, which clearly shows the alternative exposure of Mn_2O_3/C and a-Steel at the outmost surface. Besides, partial of the a-Steel was buried within the inner bulk of the Mn_2O_3/C layer (**Fig. 3f**), which could act as the cross-linked current collector to facilitate the electron transport. The EDX linear scan profiles are extracted to further confirm the material distribution at the decoupled air electrode. For the horizontal line, the signals of Mn/C and Fe/Ni exhibit staggered intensity with a unit period of 60 μm (**Fig. 3g**), manifesting the separate exposure of Mn_2O_3/C and a-Steel. For the vertical line (**Fig. 3f**), the intensity of Fe/Ni is sandwiched between intense Mn signals within 50 μm near the electrode surface, confirming the buried a-Steel within the Mn_2O_3/C layer.

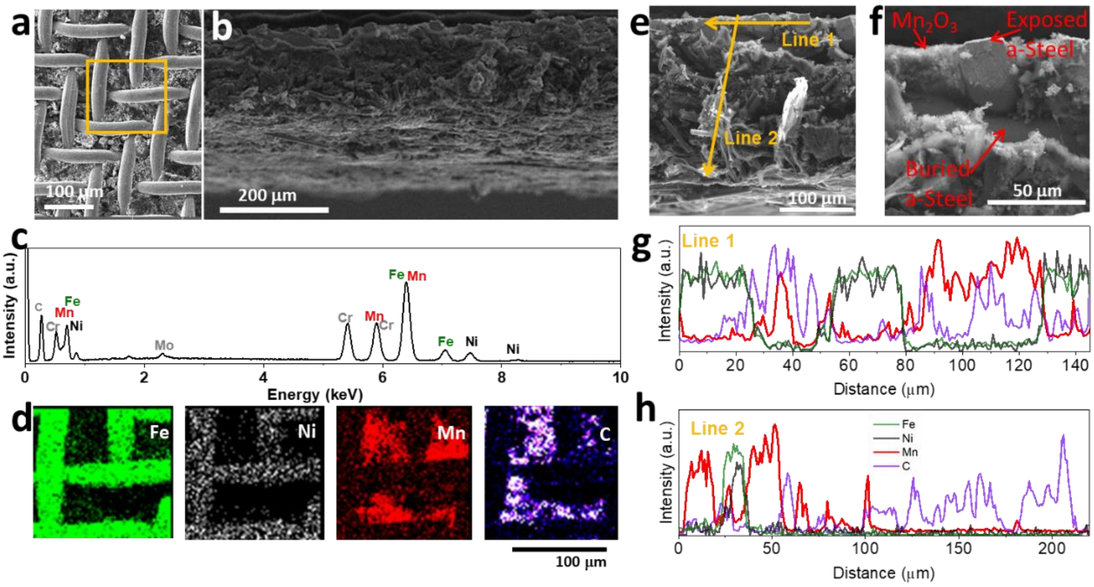

Fig. 3. Characterization of the decoupled air electrode with 400 mesh a-steel. SEM imges of (a) top view and (b) cross-section of the decoupled air electrode. (c) EDX spectrum and (d) EDX-mapping of Fe, Ni, Mn, and C of the decoupled air electrode. (e) (f) Magnified SEM image of the cross-section of the decoupled air electrode. (g) (h) EDX-linear scan of of Fe, Ni, Mn, and C distribution along Line 1 and Line 2 as labled in (e).

3.3 Adjustable hydrophobicity of the catalytic face of the decoupled air electrode

The discharge performance of the Zn-air battery is significantly influenced by the hydrophilicity of the air electrodes. By changing the mesh number of the a-Steel, the hydrophilicity of the catalytic face of the decoupled air electrode could be easily adjusted due to the variation of surface texture. From the SEM images, the conventional air electrode shows a flat surface (**Fig. 4a**), whereas the decoupled air electrodes show rougher surface due to the mesh micromorphology (**Fig. 4b-4d**).

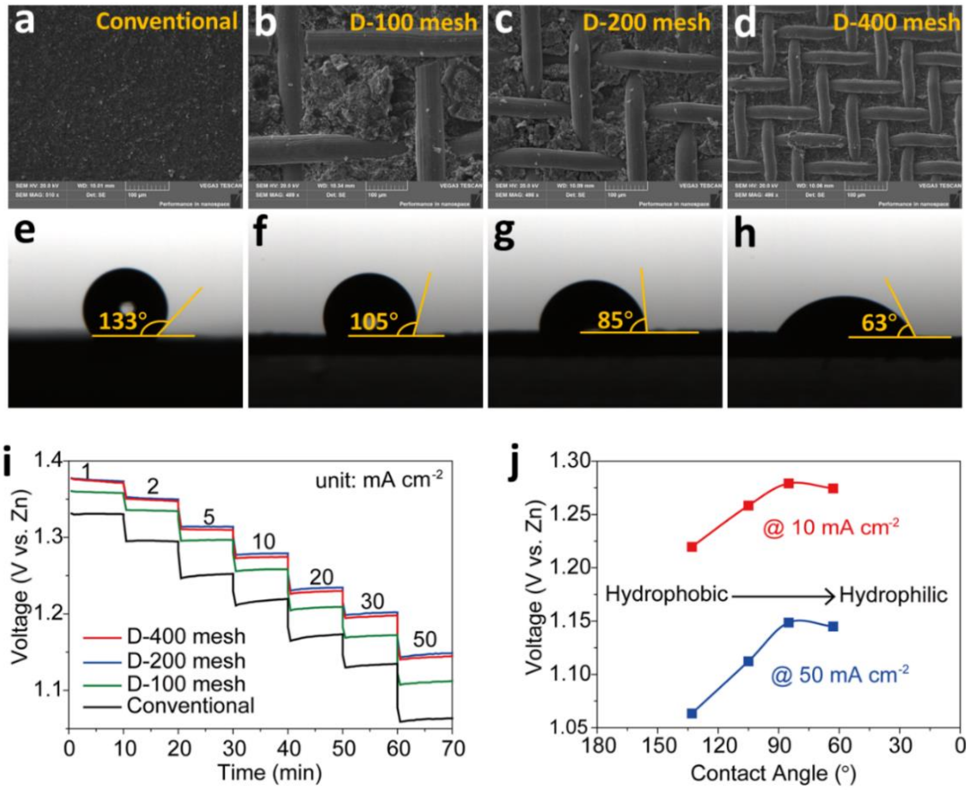

Fig. 4. Top-view SEM imges of (a) conventional air electrode, and decoupled air electrode with (b) 100 mesh, (c) 200 mesh, and (d) 400 mesh a-Steel. Contact angle of the electrocatalyst-loaded face of (e) conventional air electrode, and decoupled air electrode with (f) 100 mesh, (g) 200 mesh, and (h) 400 mesh a-Steel. (e) EDX spectrum and (d) EDX-mapping of Fe, Ni, Mn, and C of the decoupled air electrode. (i) Discharge profiles of the Zn-air battery using different air electrodes at varied current densities from 1 to 50 mA cm^{-2}. (j) Sumary of the correlation between contact angle of the catalytic surface and the discharge voltage.

The conventional air electrode exhibits the most hydrophobic surface with a contact angle of 133° (**Fig. 4e**). In comparison, the decoupled air electrode shows increased hydrophilicity due to the hydrophilic FeOOH/$Ni(OH)_2$ on a-Steel and the mesh-induced texture. Moreover, as the mesh density grows, the nano-scale roughness is increased, and the hydrophilicity increases consequently [39]. As a result, the contact angle of D-100 mesh, D-200 mesh, and D-400 mesh decreases to 105 °, 85 °, and 63 °, respectively (**Fig. 4f-4h**). Furthermore, the discharge voltages of the conventional and decoupled air electrode are recorded (**Fig. 4i**), and the relationship between the contact angle and the discharge voltage is summarized in **Fig. 4j**. The volcano shape relation between the discharge voltage and the contact angle indicates that the moderate hydrophobicity should be optimal for constructing the longest triple-phase boundary and thus providing more reacting sites for ORR during the battery discharge.

In addition to the discharge performance, the adjustable hydrophilicity also impacts the charge performance of Zn-air batteries (**Fig. 5**). By increasing the hydrophilicity of the catalytic face, the air electrodes should provide more two-phase boundary for OER due to the improved electrode-electrolyte contact [40]. To evaluate the two-phase boundary at the air electrodes for OER during battery charging, the ECSA is measured by the double layer capacitance at the electrode-electrolyte interface. The decoupled air electrodes show higher ECSA than the conventional air electrode, and the ECSA grows larger with the mesh number (**Fig. 5a-5e**). The higher hydrophilicity also leads to the decreased solution resistance as indicated by the EIS spectra (**Fig. 5f** shows the high-frequency range and **Fig. S4** shows the whole frequency range). Moreover, the decoupled air electrodes show lower charge transfer resistance than the conventional air electrode (**Table 1**), demonstrating that the partially buried a-Steel inside the powder catalyst/carbon layer can assist the electron transport. The decoupled air electrodes also deliver lower charging voltage than the conventional one, and the charge voltage reduces with the mesh number (**Fig. 5g**). It could be attributed to the increased hydrophilicity of the air electrodes and the resultant larger dual-phase boundary for OER [41,42]. During the charging test from 1 mA cm^{-2} to 50 mA cm^{-2}, concentrated OER bubbles lead to the powder catalysts/carbon peeling off from the conventional air electrode, and the peeled powder turns the electrolyte to back color as shown by the photo (**Fig. 5h**). In contrast, for the decoupled air electrodes, the OER bubbles are produced from the a-Steel and partially bypass the powder catalysts/carbon layer, thus protecting the air electrode structure. Moreover, the decreased charging voltage alleviates the oxidative carbon corrosion, which can be verified by the electrolyte color change after the charging tests (**Fig. 5h**) [2].

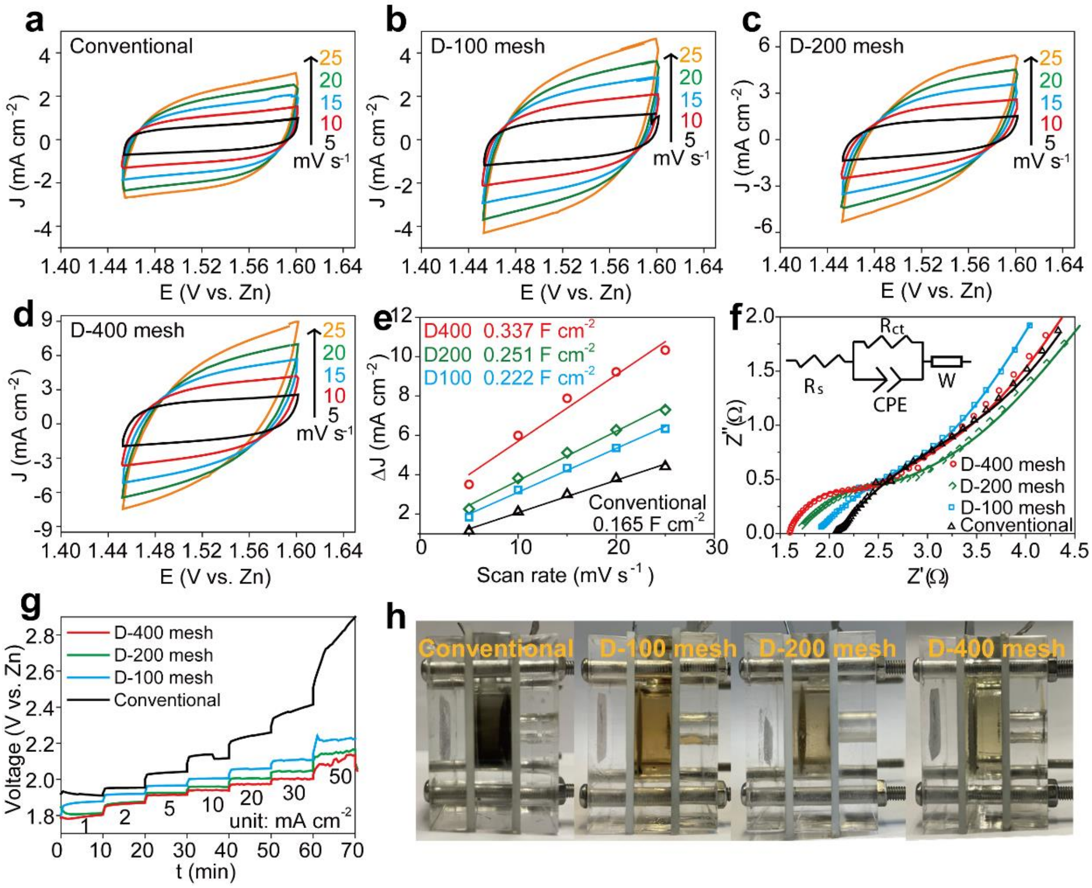

Fig. 5. The ECSA tests of (a) the conventional air electrode and the decoupled air electrode using a-Steel with (b) 100 mesh, (c) 200 mesh, (d) 400 mesh. (e) Capacitive current-scan rate relation and the C_{dl} calculation results. (f) EIS and the fitting plots of the Zn-air batteries with conventional and decoupled air electrodes. (g) Charge profiles of the Zn-air battery using different air electrodes at varied current densities from 1 to 50 mA cm^{-2}. (h) Photos of the Zn-air batteries after the charge profile tests in (g).

Table 1. EIS fittig results of the conventional air electrode and decoupled air electrodes with different mesh number.

	Rs (W)	Rct (W)
Conventional	2.07	2.10
D-100 mesh	1.83	1.01
D-200 mesh	1.55	0.28
D-400 mesh	1.47	0.27

3.4 Enhanced cycling stability of the decoupled air electrode

The D-400 mesh sample is elected to represent the decoupled air electrode for further cycling test since it shows the highest ability to resist oxidative carbon corrosion (**Fig. 5h**). The Zn-air batteries assembled using the conventional and decoupled air electrode are cycled with 3 h discharge and 3 h charge periods. When they are performed at 2 mA cm^{-2} (**Fig. 6a**), the conventional air electrode and decoupled air electrode show similar round-trip energy efficiency around 70 % at the initial cycle (**Fig. 6b**). However, the conventional air electrode shows a quick performance decay after 16 cycles (96 h), whereas the decoupled air electrode keeps a relatively stable profile for 50 cycles (300 h) with a retained energy efficiency of 63.3 %. When operated at 10 mA cm^{-2} (**Fig. 6c**), the conventional air electrode shows an initial voltage gap of 0.89 V with energy efficiency of 56.2 %. In comparison, the decoupled air electrode delivers a much better performance with initial voltage gap of 0.75 V and energy efficiency of 62.6 %. In addition, the decoupled air electrode also shows good cycle stability at 10 mA cm^{-2} for 40 cycles (240 h) and preserves a voltage gap of 0.92 V and energy efficiency of 54.2 %, whereas the conventional air electrode shows rapid voltage gap increasement in only 8 cycles (48 h) with retained energy efficiency of only 40% (**Fig. 6d**).

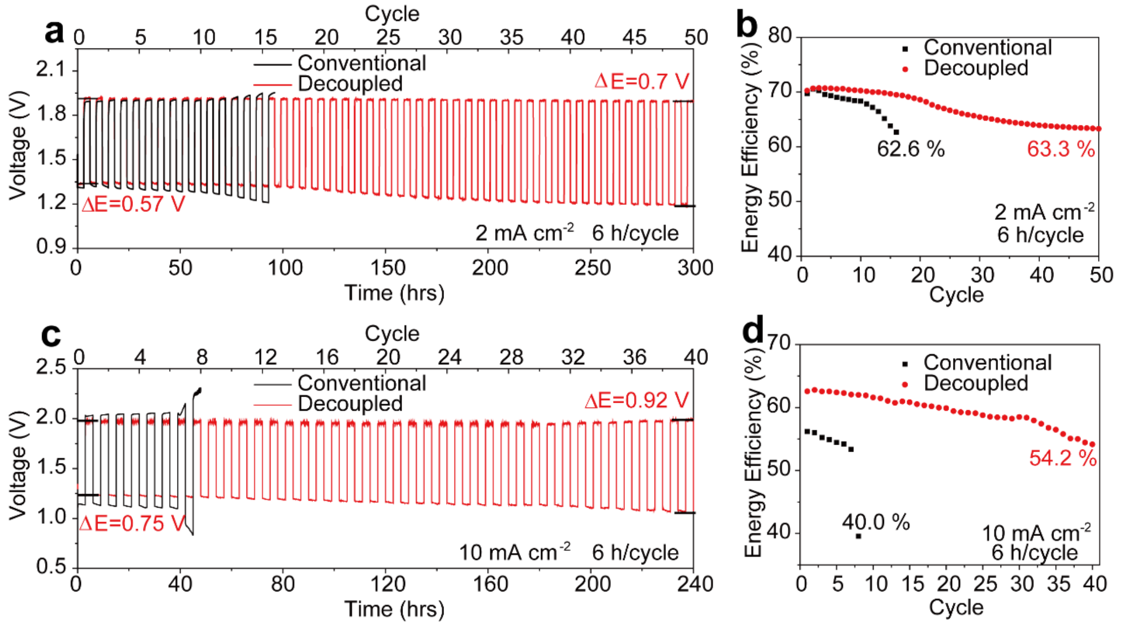

Fig. 6. Galvanostatic charge-discharge profiles of Zn-air batteries cycled at (a) 2mA cm^{-2} and (c) 10 mA cm^{-2}. Round-trip energy effciencies of Zn-air batteries along cycling operation at (b) 2mA cm^{-2} and (d) 10 mA cm^{-2}.

Furthermore, the decoupled air electrode was performed in ZnO saturated 6 M KOH electrolyte (**Fig. S5).** It shows the stable cycling profile at 10 mA cm^{-2} for 40 cycles (240 h), which is close to the result tested in the non-ZnO electrolyte, indicating that the ZnO does not impact the performance of the decoupled air electrode. In addition, the conventional air electrode fabricated by the noble metal benchmark Pt/C+RuO_2 was also cycled at 10 mA cm^{-2} (**Fig. S6**). Although it shows the high initial energy efficiency of 66.6 % at the 1st cycle, it quickly decays to 36.8 % at the 20th cycle, showing a significantly shorter lifespan than the decoupled air electrode using the Ni/Fe/Mn-based materials. This control experiment further confirms that the decoupled structure could efficiently improve the cycle stability of the air electrode, making the low-cost materials more competitive in the Zn-air battery application.

The cycled electrodes are further characterized for a deeper understanding of the superior stability of the decoupled air electrode. The XRD patterns of both conventional and decoupled electrodes (**Fig. S7**) show that the catalysts preserve the original crystal structure after battery cycling, and thus the performance decay is not due to the phase change of catalysts. **Fig. 7a** compares the Mn 2p XPS spectra of the original Mn_2O_3, the catalytic face of the conventional and decoupled air electrodes after cycling at 10 mA cm^{-2} for 8 cycles (48 h). The cycled conventional air electrode shows a significantly increased binding energy of Mn 2p$_{3/2}$ (642.5 eV) as compared to the original Mn_2O_3 (642.0 eV), implying the oxidation of Mn during the battery cycling. In contrast, the cycled decoupled air electrode retains the same peak position of Mn 2p$_{3/2}$ (642.0 eV) as compared to the original Mn_2O_3, indicating the unchanged valence state of Mn. The results confirm that decoupled air electrode structure can protect the ORR catalyst from oxidative corrosion.

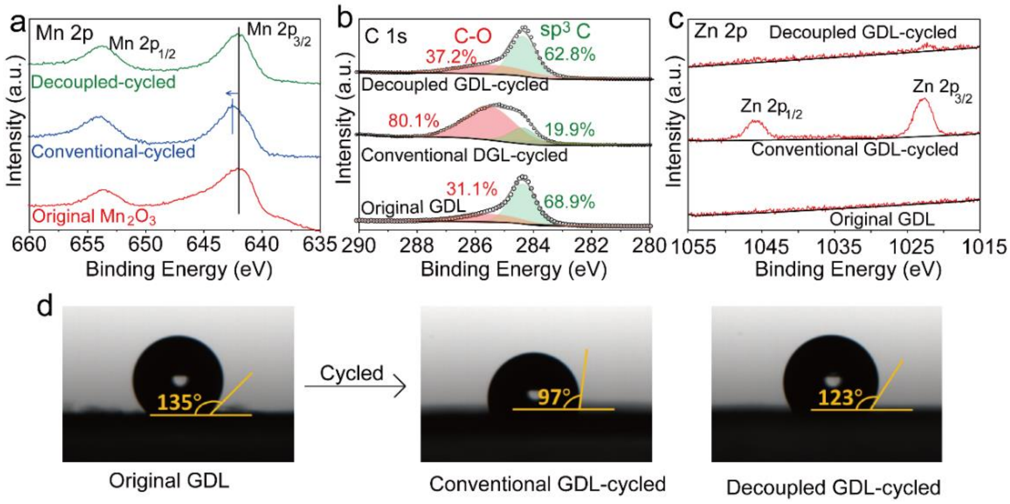

Fig. 7. (a) Mn 2p XPS spectra of the original Mn_2O_3 and the catalytic face of the cycled conventional and decoupled air electrodes. (b) C 1s and (c) Zn 2p XPS sectra of original GDL and the GDL of the cycled conventional and electrodes. (d) Contact angle of the of the original GDL and the GDL of the cycled convential and decoupled air electrodes.

Besides, the oxidative corrosion of the GDL during battery cycling is studied in **Fig. 7 (b-d),** which compare the original GDL, the air face of the conventional air electrode after 16 cycles (96 h) at 2 mA cm^{-2}, and the air face of decoupled air electrode after 20 cycles (120 h) at 2 mA cm^{-2}. For the C 1s XPS spectra (**Fig. 7b**), the original

GDL shows C-O and sp^3 C species with the ratios of 31.1% and 68.9%, respectively. The cycled conventional air electrode shows greatly enhanced C-O of 80.1% indicating significant oxidative corrosion. In contrast, the cycled decoupled air electrode shows slightly increased C-O ratio of 37.2% implying the rather low degree of the oxidative corrosion. Moreover, the XPS spectrum of Zn 2p (**Fig. 7c**) is acquired to investigate the flooding of electrolyte through the air electrodes. The original GDL shows no signal of Zn. In contrast, the cycled conventional air electrode shows obvious Zn signal that indicates severe electrolyte flooding. In comparison, the cycled decoupled air electrode shows very weak Zn signal, implying that the electrolyte flooding is reduced.

Furthermore, the evaluation of hydrophilicity of the air face of the air electrodes along cycling was scrutinized by the contact angle measurement (**Fig. 7d**). The original GDL shows a hydrophobic air face with the contact angle of 135º, which guarantees the diffusion pathway of the O_2 gas. The cycled conventional air electrode displays more hydrophilic air face with largely decreased contact angle of 97º, further manifesting the serious carbon corrosion [43], which could inhibit the gas diffusion. In comparison, the cycled decoupled air electrode still preserves a relatively hydrophobic air face with contact angle of 123º, indicating the maintained gas diffusion pathway along cycling. The above analysis demonstrates that the unique structure of decoupled air electrode could efficiently inhibit the oxidative corrosion of the air electrode, and thus prevents the electrolyte flooding and persists the gas diffusion pathway along cycling. Therefore, the decoupled air electrode shows promoted cycle stability as compared to the conventional one.

4. Conclusions

In summary, an air electrode with decoupled ORR-OER sites is fabricated by a facile method of pressing a hydrophilic OER-mesh and a hydrophobic ORR layer. The hydrophobicity of the catalytic surface could be adjusted by changing the texture of the steel mesh. The decoupled air electrode achieves the optimal discharge performance at the moderate contact angle of about 85 º, which is due to the balance of electrode contact with gas and liquid phase, and the resultant abundant triple-phase boundary for ORR reaction. Furthermore, the decoupled structure could separate the OER and ORR sites at microscale, which alleviates the oxidative corrosion of carbon component of the air electrode during charging process, and thus enhances the cycle stability of Zn-air battery. This work provides a facile strategy to simultaneously engineer the abundance and distribution of reaction sites, which might be instructive for a wide range of electrochemical energy storage and conversion devices.

Acknowledgement

This work is supported by a grant from Collaborative Research Fund (CRF) (Project no. C5031-20G) of Research Grant Council, University Grants Committee, HK SAR. P. Tan thanks the funding support from Anhui Provincial Natural Science Foundation (2008085ME155) and USTC Research Funds of the Double First-Class Initiative (YD2090002006). We thank Professor Zijian Zheng from Institute of Textiles & Clothing of The Hong Kong Polytechnic University for the discussing, chemical support, and the contact angle test.

Declaration of competing interests

The authors declare no conflict of interests.

References

[1] S. Chu, A. Majumdar, Opportunities and challenges for a sustainable energy future, Nature 488 (2012) 294-303.

[2] Q. Lu, Y. Guo, P. Mao, K. Liao, X. Zou, J. Dai, P. Tan, R. Ran, W. Zhou, M. Ni, Rich atomic interfaces between sub-1 nm RuO_x clusters and porous Co_3O_4 nanosheets boost oxygen electrocatalysis bifunctionality for advanced Zn-air batteries, Energy

Storage Mater. 32 (2020) 20-29.
[3] P. Tan, B. Chen, H. Xu, W. Cai, W. He, M. Ni, Porous Co_3O_4 nanoplates as the active material for rechargeable Zn-air batteries with high energy efficiency and cycling stability, Energy 166 (2019) 1241-1248.
[4] W. Sun, F. Wang, B. Zhang, M. Zhang, V. Küpers, X. Ji, C. Theile, P. Bieker, K. Xu, C. Wang, A rechargeable zinc-air battery based on zinc peroxide chemistry, Science 371 (2021) 46-51.
[5] W. Yu, W. Shang, X. Xiao, P. Tan, B. Chen, Z. Wu, H. Xu, M. Ni, Achieving a stable zinc electrode with ultralong cycle life by implementing a flowing electrolyte, J. Power Sources 453 (2020) 227856.
[6] Q. Zhang, J. Guan, Applications of Atomically Dispersed Oxygen Reduction Catalysts in Fuel Cells and Zinc–Air Batteries, Energy Environ. Mater. 4 (2021) 307-335.
[7] X. Liu, G. Zhang, L. Wang, H. Fu, Structural Design Strategy and Active Site Regulation of High‐Efficient Bifunctional Oxygen Reaction Electrocatalysts for Zn–Air Battery, Small (2021) 2006766.
[8] J. Yu, R. Ran, Y. Zhong, W. Zhou, M. Ni, Z. Shao, Advances in porous perovskites: synthesis and electrocatalytic performance in fuel cells and metal–air batteries, Energy Environ. Mater. 3 (2020) 121-145.
[9] Q. Shi, Q. Liu, Y. Zheng, Y. Dong, L. Wang, H. Liu, W. Yang, Controllable Construction of Bifunctional Co_xP@N, P‐Doped Carbon Electrocatalysts for Rechargeable Zinc‐Air Batteries, Energy Environ. Mater. 0 (2021).
[10] P. Tan, B. Chen, H. Xu, W. Cai, W. He, M. Liu, Z. Shao, M. Ni, Co_3O_4 nanosheets as active material for hybrid Zn batteries, Small 14 (2018) 1800225.
[11] C. Tang, H.-F. Wang, Q. Zhang, Multiscale principles to boost reactivity in gas-involving energy electrocatalysis, Acc. Chem. Res. 51 (2018) 881-889.
[12] Y.-C. Wang, L. Huang, P. Zhang, Y.-T. Qiu, T. Sheng, Z.-Y. Zhou, G. Wang, J.-G. Liu, M. Rauf, Z.-Q. Gu, Constructing a triple-phase interface in micropores to boost performance of Fe/N/C catalysts for direct methanol fuel cells, ACS Energy Lett. 2 (2017) 645-650.
[13] Z. J. Xu, From two-phase to three-phase: the new electrochemical interface by oxide electrocatalysts, Nano-Micro Lett. 10 (2018) 1-3.
[14] S. She, Y. Zhu, H. A. Tahini, Z. Hu, S.-C. Weng, X. Wu, Y. Chen, D. Guan, Y. Song, J. Dai, A molecular-level strategy to boost the mass transport of perovskite electrocatalyst for enhanced oxygen evolution, Appl. Phys. Rev. 8 (2021) 011407.
[15] L. Pan, D. Chen, P. Pei, S. Huang, P. Ren, X. Song, A novel structural design of air cathodes expanding three-phase reaction interfaces for zinc-air batteries, Appl. Energy 290 (2021) 116777.

[16] D. Lee, H. Lee, O. Gwon, O. Kwon, H. Y. Jeong, G. Kim, S.-Y. Lee, Monolithic heteronanomat paper air cathodes toward origami-foldable/rechargeable Zn–air batteries, J. Mater. Chem. A 7 (2019) 24231-24238.
[17] B. Liu, Y.-K. Dai, L. Li, H. D. Zhang, L. Zhao, F.-R. Kong, X.-L. Sui, Z. B. Wang, Effect of polytetrafluoroethylene (PTFE) in current collecting layer on the performance of zinc-air battery, Progress in Natural Science: Materials International 30 (2020) 861-867.
[18] Y. Dai, J. Yu, M. Ni, Z. Shao, Rational design of spinel oxides as bifunctional oxygen electrocatalysts for rechargeable Zn-air batteries, Chem. Phys. Rev. 1 (2020) 011303.
[19] P. Tan, B. Chen, H. Xu, W. Cai, W. He, M. Ni, Investigation on the electrode design of hybrid Zn-Co_3O_4/air batteries for performance improvements, Electrochim. Acta 283 (2018) 1028-1036.
[20] J. Yu, B. Q. Li, C. X. Zhao, J. N. Liu, Q. Zhang, Asymmetric air cathode design for enhanced interfacial electrocatalytic reactions in high‐performance zinc‐air batteries, Adv. Mater. 32 (2020) 1908488.
[21] J. Li, Y. Zhu, W. Chen, Z. Lu, J. Xu, A. Pei, Y. Peng, X. Zheng, Z. Zhang, S. Chu, Breathing-mimicking electrocatalysis for oxygen evolution and reduction, Joule 3 (2019) 557-569.
[22] Y. Zhong, X. Xu, P. Liu, R. Ran, S. P. Jiang, H. Wu, Z. Shao, A Function‐Separated Design of Electrode for Realizing High‐Performance Hybrid Zinc Battery, Adv. Energy Mater. 10 (2020) 2002992.
[23] T. Zhou, N. Zhang, C. Wu, Y. Xie, Surface/interface nanoengineering for rechargeable Zn–air batteries, Energy Environ. Sci. 13 (2020) 1132-1153.
[24] Y. Wang, Q. Cao, C. Guan, C. Cheng, Recent Advances on Self‐Supported Arrayed Bifunctional Oxygen Electrocatalysts for Flexible Solid‐State Zn‐Air Batteries, Small 16 (2020) 2002902.
[25] Y. Arafat, M. R. Azhar, Y. Zhong, X. Xu, M. O. Tadé, Z. Shao, A Porous Nano-micro-composite as a high-performance bi-functional air electrode with remarkable stability for rechargeable zinc–air batteries, Nano-Micro Lett. 12 (2020) 1-16.
[26] Y. He, W. Shang, M. Ni, Y. Huang, H. Zhao, P. Tan, In-Situ Observation of the Gas Evolution Process on the Air Electrode of Zn-Air Batteries during Charging, Chem. Eng. J. (2021) 130862.
[27] S. G. Ji, H. Kim, W. H. Lee, H.-S. Oh, C. H. Choi, Real-time monitoring of electrochemical carbon corrosion in alkaline media, J. Mater. Chem. A (2021).
[28] H. Li, L. Ma, C. Han, Z. Wang, Z. Liu, Z. Tang, C. Zhi, Advanced rechargeable zinc-based batteries: Recent progress and future perspectives, Nano Energy 62 (2019) 550-587.

[29] A. R. Ugalde, H. E. Naguib, Double-layer membrane cathode with improved oxygen diffusivity in zinc-air batteries, Energy Storage Mater. 8 (2017) 1-9.
[30] M. Xiong, M. P. Clark, M. Labbe, D. G. Ivey, A horizontal zinc-air battery with physically decoupled oxygen evolution/reduction reaction electrodes, J. Power Sources 393 (2018) 108-118.
[31] K. Wang, C. Liao, W. Wang, Y. Xiao, X. Liu, S. Zhao, Physical shortcut accelerating electron transport of rechargeable zinc-air battery, Mater. Today Energy 14 (2019) 100340.
[32] W. Hong, H. Li, B. Wang, A horizontal three-electrode structure for zinc-air batteries with long-term cycle life and high performance, Int. J. Electrochem. Sci 11 (2016) 3843-3851.
[33] P. Wang, Y. Lin, L. Wan, B. Wang, Construction of a janus MnO_2-NiFe electrode via selective electrodeposition strategy as a high-performance bifunctional electrocatalyst for rechargeable zinc–air batteries, ACS applied materials interfaces 11 (2019) 37701-37707.
[34] Y. Wang, Y. Zhu, S. Zhao, S. She, F. Zhang, Y. Chen, T. Williams, T. Gengenbach, L. Zu, H. Mao, Anion etching for accessing rapid and deep self-reconstruction of precatalysts for water oxidation, Matter 3 (2020) 2124-2137.
[35] G. Chen, Y. Zhu, H. M. Chen, Z. Hu, S. F. Hung, N. Ma, J. Dai, H. J. Lin, C. T. Chen, W. Zhou, An amorphous nickel‐iron‐based electrocatalyst with unusual local structures for ultrafast oxygen evolution reaction, Adv. Mater. 31 (2019) 1900883.
[36] S. Wang, Q. Liu, Z. Zhao, C. Fan, X. Chen, G. Xu, M. Wu, J. Chen, J. Li, Enhanced low-temperature activity of toluene oxidation over the rod-like $MnO_2/LaMnO_3$ perovskites with alkaline hydrothermal and acid-etching treatment, Ind. Eng. Chem. Res. 59 (2020) 6556-6564.
[37] K. Zhu, W. Luo, G. Zhu, J. Wang, Y. Zhu, Z. Zou, W. Huang, Interface‐Engineered Ni $(OH)_2/\beta$‐like FeOOH Electrocatalysts for Highly Efficient and Stable Oxygen Evolution Reaction, Chem. Asian J. 12 (2017) 2720-2726.
[38] K.-H. Kim, D. K. Lee, Y.-H. Choi, Fabrication of Single-Phase Manganese Oxide Films by Metal-Organic Decomposition, Materials 14 (2021) 2338.
[39] P. Yiu, J.-D. You, S.-T. Wang, J. P. Chu, Tunable hydrophilicity in a surface nano-textured stainless steel thin film deposited by DC magnetron sputtering, Appl. Surf. Sci. 555 (2021) 149705.
[40] J. Liu, H. Yuan, Z. Wang, J. Li, M. Yang, L. Cao, G. Liu, D. Qian, Z. Lu, Self-supported nickel iron oxide nanospindles with high hydrophilicity for efficient oxygen evolution, Chem. Commun. 55 (2019) 10860-10863.
[41] Y. Wei, C.-H. Shin, E. B. Tetteh, B.-J. Lee, J.-S. Yu, Insight into the boosted electrocatalytic oxygen evolution performance of highly hydrophilic nickel–iron

hydroxide, ACS Appl. Energy Mater. 3 (2019) 822-830.
[42] J. Zhao, X. Quan, S. Chen, Y. Liu, H. Yu, Cobalt nanoparticles encapsulated in porous carbons derived from core–shell ZIF67@ ZIF8 as efficient electrocatalysts for oxygen evolution reaction, ACS applied materials interfaces 9 (2017) 28685-28694.
[43] Y. Yi, G. Weinberg, M. Prenzel, M. Greiner, S. Heumann, S. Becker, R. Schlögl, Electrochemical corrosion of a glassy carbon electrode, Catal. Today 295 (2017) 32-40.